

The metallicity gradient of M 33: chemical abundances of H II regions [★]

L. Magrini¹, J. M. Vílchez², A. Mampaso³, R.L.M. Corradi^{4,3}, P. Leisy^{4,3}

¹ INAF-Osservatorio Astrofisico di Arcetri, Largo E. Fermi, 5, 50125 Firenze, Italy

² Instituto de Astrofísica de Andalucía (CSIC) Apartado de Correos 3004, 18080 Granada, Spain

³ Instituto de Astrofísica de Canarias, c. Vía Láctea s/n, 38200, La Laguna, Tenerife, Canarias, Spain

⁴ Isaac Newton Group of Telescopes, Apartado de Correos 321, 38700 Santa Cruz de La Palma, Canarias, Spain

Received ; accepted

ABSTRACT

Context. We present spectroscopic observations of a sample of 72 emission-line objects, including mainly H II regions, in the spiral galaxy M 33. Spectra were obtained with the multi-object, wide field spectrograph AF2/WYFFOS at the 4.2m WHT telescope. Line intensities, extinction, and electron density were determined for the whole sample of objects.

Aims. The aim of the present work was to derive chemical and physical parameters of a set of H II regions, and from them the metallicity gradient.

Methods. Electron temperatures and chemical abundances were derived for the 14 H II regions where both [O II] and [O III] emission line fluxes were measured, including the electron temperature sensitive emission line [O III] 436.3 nm and in a few cases [N II] 575.5 nm. The ionization correction factor (ICF) method was used to derive the total chemical abundances.

Results. The presence of abundance gradients was inferred from the radial behaviour of several emission-line ratios, and accurately measured from chemical abundances directly derived in 14 H II regions. The oxygen abundances of our H II regions, located in the radial region from ~ 2 to ~ 7.2 kpc, gave an oxygen gradient -0.054 ± 0.011 dex kpc⁻¹.

Conclusions. The overall oxygen gradient for M 33 obtained using ours and previous oxygen determinations in a large number of H II regions with direct electron temperature determination as well as abundance in young stars presented a two slope shape: -0.19 dex kpc⁻¹ for the central regions ($R < 3$ kpc), and -0.038 dex kpc⁻¹ for the outer regions ($R \geq 3$ kpc).

Key words. Galaxies: abundances, evolution - Galaxies, individual: M33 - ISM: abundances, HII regions

1. Introduction

The galaxy M 33 (NGC 598) is the third-brightest member of the Local Group. Its closeness (840 kpc, Freedman et al. 1991), its large angular size (optical size $53' \times 83'$, Holmberg 1958), and its intermediate inclination ($i=53^\circ$) make it particularly suitable for studies of spiral structure, interstellar medium (ISM), and of stellar populations (van den Bergh 2000). Being a late-type spiral galaxy, it has a rich population of H II regions. A catalog of large-sized H II regions was given by Courtes et al. (1987), whereas the positions of compact H II regions were published by Calzetti et al. (1995). One of the most recent catalogs, published in two part by Wyder et al. (1997) and Hodge et al. (1999), lists a large number of new H II regions. Observations with the 2.5 m INT telescope at La Palma, Spain, covering an area of approximately 0.6 square degrees, produced the most complete catalog of H II regions in this galaxy (Cardwell et al. 2000). Recently, the Local Group Census consortium (LGC <http://www.ing.iac.es/~rcorradi/LGC/>, cf. Corradi & Magrini 2006) obtained new imaging observations of M 33. These new deep data cover about 2 square degrees and are al-

lowing to discover a conspicuous number of new H II regions at large galactocentric distances.

The existence of chemical abundance gradients in M 33 was known from long time, but its origin, shape and magnitude are still open issues. Aller (1942) noted that among H II regions in M33, those far from the center had much larger [O III]/[O II] emission line ratios than those near the center. Searle (1971) presented spectrophotometry of eight H II regions in M 33 and recognized that a radial abundance gradient could explain this trend of flux ratios.

Further spectroscopic studies of H II regions were carried on by Smith (1975), Kwitter & Aller (1981), and by Vílchez et al. (1988). Garnett et al. (1997) in a recompilation of previous observations, obtained an overall O/H gradient of -0.11 ± 0.02 dex kpc⁻¹. Willner & Nelson-Patel (2002) derived neon abundances of 25 H II regions from infrared lines, obtaining a Ne/H gradient -0.05 ± 0.02 dex kpc⁻¹. A new recompilation of young stars and H II regions abundance determinations was done also by Pérez-Montero & Díaz (2005). Recently, Crockett et al. (2006) derived even shallower gradients (Ne/H -0.016 ± 0.017 dex kpc⁻¹, and O/H -0.012 ± 0.011 dex kpc⁻¹) using chemical abundances of 6 H II regions with derived electron temperature.

The abundance gradient of M 33 was also investigated using planetary nebulae (PNe), young giant stars, and red giant branch (RGB) stars. PNe chemical abundances were studied by Magrini et al. (2004) via optical spectroscopy and photoioniza-

Send offprint requests to: L. Magrini
e-mail: laura@arcetri.astro.it

[★] Based on observations obtained at the 4.2m WHT telescope operated on the island of La Palma by the Isaac Newton Group in the Spanish Observatorio del Roque de Los Muchachos of the Instituto de Astrofísica de Canarias.

tion modelling and by Stasinska et al. (2006) with direct electron temperature measurements of PNe located in the inner regions of M 33. Stellar abundances were obtained by Herrero et al. (1994) for AB-supergiants, McCarthy et al. (1995) and Venn et al. (1998) for A-type supergiant stars, and Monteverde et al. (1997, 2000) and Urbaneja et al. (2005) for B-type supergiant stars. The O/H gradient as derived by Urbaneja et al. (2005) is -0.06 ± 0.02 dex kpc^{-1} . The metallicity measured in Cepheids identified in the inner regions of M 33 by Beaulieu et al. (2006) suggested an O/H gradient of -0.16 dex kpc^{-1} . Metallicities of old stellar populations were derived via deep CCD photometry and colour magnitude diagrams by Stephens & Frogel (2002), Kim et al. (2002), Galletti et al. (2004), Tiede et al. (2004), Brooks et al. (2004), and Barker et al. (2006). The [Fe/H] gradient computed by Barker et al. (2006) including all previous iron determinations in RGB stars was -0.07 ± 0.01 dex kpc^{-1} .

The aim of the present paper is to investigate the chemical and physical properties of a large sample of H II regions of different sizes, galactocentric distances and excitations and to study their behaviour through the disk.

The paper is organized as follows: in Sect. 2 we present observations and data reductions, while in Sect. 3 we discuss the behaviour of the extinction across the disk. Emission-line ratio diagrams are shown in Sect. 4 and the physical and chemical properties of the studied H II regions are presented in Sect. 5. The metallicity gradients and their implication in the evolution of M 33 are discussed in Sect. 6 and in Sect. 7. Finally in Sect. 8 we summarize our conclusions.

2. Observations and data reduction

Seventy-two emission-line objects (see Fig. 1) were observed on November 18th and 19th, 2004 with AF2/WYFFOS, the multi-object, wide field, fibre spectrograph working at the prime focus of the 4.2 m William Herschel Telescope (La Palma, Spain) equipped with an Atmospheric Dispersion Corrector that corrects for the effect of atmospheric dispersion. We used a 1024×1024 TEK CCD, and the Small Fibre module which contains 150 science fibres with $1.6''$ diameter ($90 \mu\text{m}$) projected on the sky. The WYFFOS spectrograph was used with a single setup: R600B grating (600 line mm^{-1}) providing a dispersion of 3.0 \AA pix^{-1} . The observations were repeated with two different incidence angles and consequently two different central wavelengths were obtained: 513 nm and 574 nm. The resulting total spectral coverage ranged from approximately 370.0 nm to 750.0 nm, and included the basic lines needed for the classification of the objects and the determination of their physical and chemical properties. The response of the instrument in the bluer part of the spectra ($<400.0 \text{ nm}$) was inadequate and thus not suitable for further analysis. We have considered the spectral range from 410.0 nm to 750.0 nm for the subsequent work.

The positions of our targets were obtained from the INT+WFC images by Magrini et al. (2000) and from Local Group Census (LGC) observations (Corradi & Magrini 2006). The selection criteria for the observed sample of emission-line objects, including mostly H II regions, but also PNe and SNRs, were the following: *i*) uniform distribution over the face of the galaxy; *ii*) large range of sizes and shapes; *iii*) bright [O III] $\lambda 500.7 \text{ nm}$ emission in order to make possible the chemical abundance determination. We aimed to contribute to the study of the metallicity gradient in M 33 with a sample of H II regions of different morphological types and sizes, selecting for observation H II regions without previous spectroscopic data, avoiding to repeat the study of already well analyzed giant H II regions.

The coordinates, classifications and fluxes in previous catalogs, when available, are shown in Table 1. The 13 emission-line objects not identified in previous works, mostly small isolated H II regions, are labeled with LGC-HII-n, standing for H II regions discovered by the LGC project. The $\text{H}\alpha + [\text{N II}]$ fluxes of these H II regions were computed using aperture photometry in the INT+WFC images by Magrini et al. (2000).

A total of 6 science exposures of 1800 s each were taken with the central wavelength $\lambda 513 \text{ nm}$, and with a mean airmass 1.1, and 3 exposures of 1800 s at $\lambda 574 \text{ nm}$, with a mean airmass 1.4. The seeing during the observations was $1.5''$ during the first night and $<1''$ in the second night. Several offset sky exposures using the same fibre configuration were taken before and after the M 33 observations to perform sky subtraction. Twilight sky and tungsten lamp exposures were taken as flat fields, while helium and neon lamp exposures were used for wavelength calibration.

The data were reduced using the IRAF¹ multi-fibre spectra reduction package DOFIBER. The data reduction of a similar set of observations, and in particular the sky subtraction procedure, were described in detail in Magrini et al. (2003). Here we remind briefly the sky subtraction process. The sky spectra were taken in two different ways: *i*) with sky fibres taken during the exposures of M 33, that served to monitor the relative intensity of the atmospheric emission lines, which are known to vary during the night, *ii*) with offset-sky spectra that allowed to control the variations in the instrumental profiles of the position of each individual fibre in the focal plane. The final sky subtraction was done using the offset-sky spectra, after correcting their relative intensity of the atmospheric lines using the mean sky spectrum computed from the sky fibres observed at the same time as the science targets. Relative flux calibration was obtained taking spectra with several fibres of the spectrophotometric standard stars HD 93521 and BD+25 4655 (Oke 1990). All standard stars were observed with airmass <1.1 . The feasibility of the use of a mean sensitivity function for all the fibres was demonstrated by Magrini et al. (2003). Emission line fluxes were measured using the IRAF SPLIT package. Errors in the fluxes were calculated taking into account the statistical error in the measurement of the fluxes, as well as systematic errors of the flux calibrations, background determination, and sky subtraction. The observed emission line fluxes and their errors are listed in Tab. 2.

3. The extinction

The observed line fluxes were corrected for the effect of the internal and interstellar extinction. The extinction law of Mathis (1990) with $R_V=3.1$ was used. The $c(\text{H}\beta)$, which measures the logarithmic difference between the observed and un-reddened $\text{H}\beta$ fluxes, was determined comparing the observed Balmer $I(\text{H}\alpha)/I(\text{H}\beta)$ ratio with its theoretical value. The effect of the underlying absorption from the continuum below the Balmer lines was neglected. The extinction coefficients $c(\text{H}\beta)$ for the complete sample of H II regions are shown in Tab. 2.

In Fig. 2, the radial dependence of the extinction, converted in $E(\text{B}-\text{V})$ with the relation $c(\text{H}\beta)=0.4 R_\beta E(\text{B}-\text{V})$, where $R_\beta=3.7$, is reported. We remind that in this plot and in the following diagrams the adopted distance to M 33 is 840 kpc (Freedman et al. 1991). The figure shows the histogram of the mean extinc-

¹ IRAF is distributed by the National Optical Astronomy Observatories, which are operated by the Association of Universities for Research in Astronomy, Inc., under cooperative agreement with the National Science Foundation.

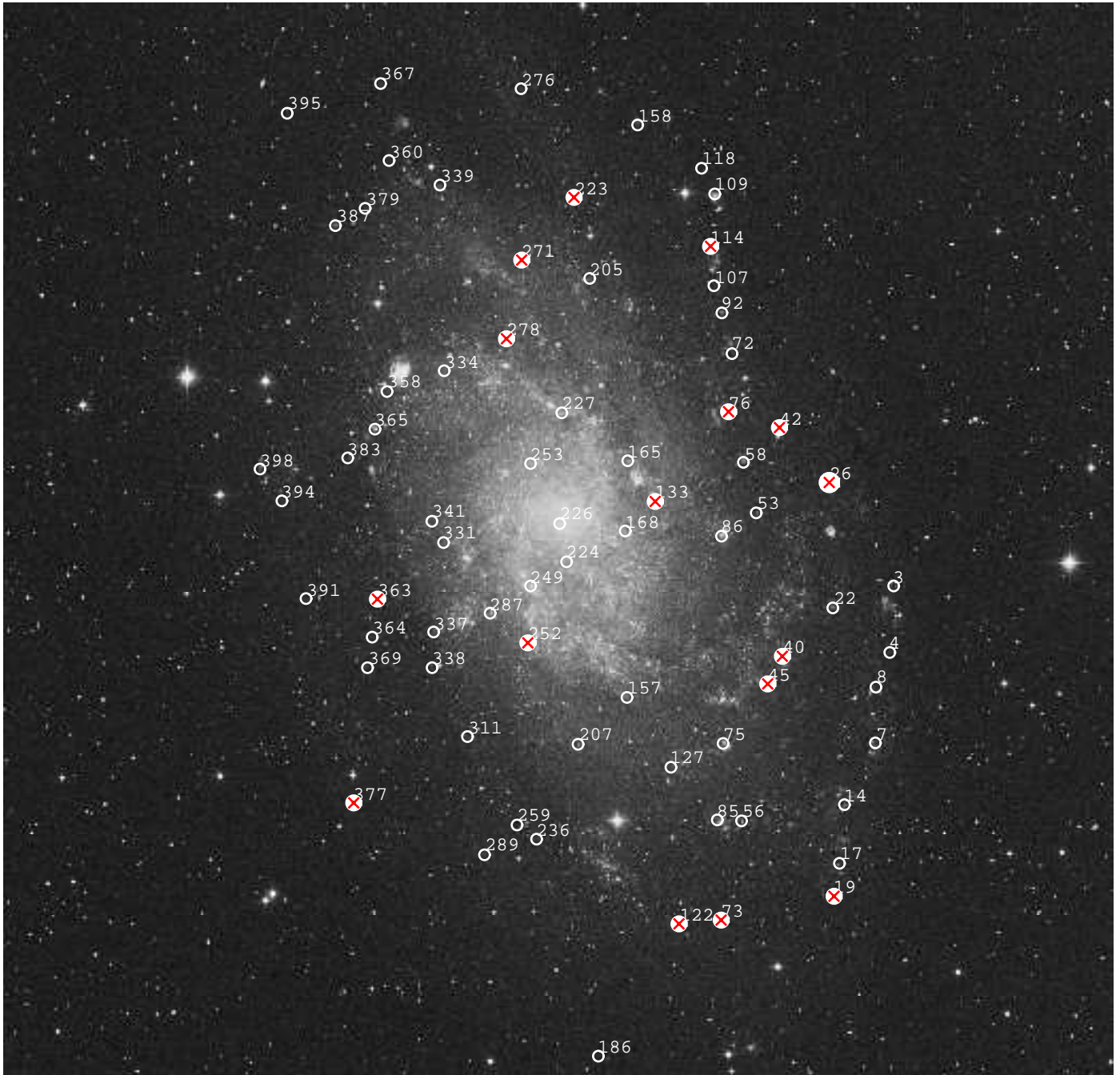


Fig. 1. M33 DSS $1^\circ \times 1^\circ$ image indicating the location of the 72 observed emission-line objects (North is up and East to the left). The labeled id correspond to the first column of Table 1. H II regions with measured chemical abundances are marked with a cross.

tion in each 2 kpc bin from the centre of the galaxy. The error is the *rms* scatter of the average of the values of the extinction in each bin. Note an almost uniform trend of the extinction, with an average value across the whole disk of $\langle E(B-V) \rangle = 0.22 \pm 0.15$, corresponding to $A_V = 0.65$.

In Fig. 3, the radial dependence of the extinction in four quadrants of M 33 is also shown: NE north-east, NW north-west, SE south-east, and SW south-west. The extinction was computed as described for Fig. 2. The point in the first bin of the SW quadrant is not very representative being the average of only two H II regions extinctions. Note that the nebulae located in the eastern part of the galaxy present a lower average extinction. This might be attributed to the effect of the inclination of M 33. The east-

ern parts of the galaxy are indeed the farther ones, and because of an effect of projection, dust filaments are observed below the H II regions, while in the western regions, because of the same effect, the dust is located above the H II regions, thus enhancing the total extinction.

Previous work by Viallefond & Goss (1986) and by Israel & Kennicutt (1980) examined the extinction behaviour in a sample of H II regions of M 33. They both found that the extinction derived from Balmer lines is smaller than the extinction obtained from radio free-free and Balmer line comparison. This is due to a non uniform distribution of dust inside the H II regions, together with the different part of the nebula monitored by the two methods: the first method is more sensitive to the extinction in the

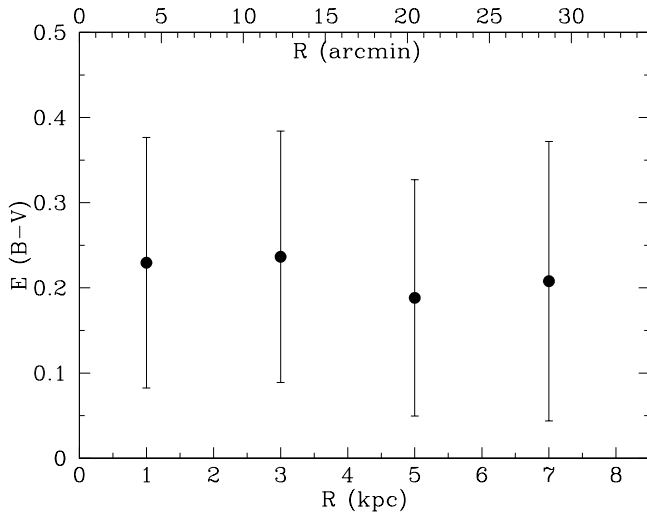


Fig. 2. The radial dependence of the extinction, converted from $c(H\beta)$ to $E(B-V)$ with the relation $c(H\beta)=0.4 R_\beta E(B-V)$, where $R_\beta=3.7$. The *filled circles* are the mean extinction in each 2 kpc wide bin.

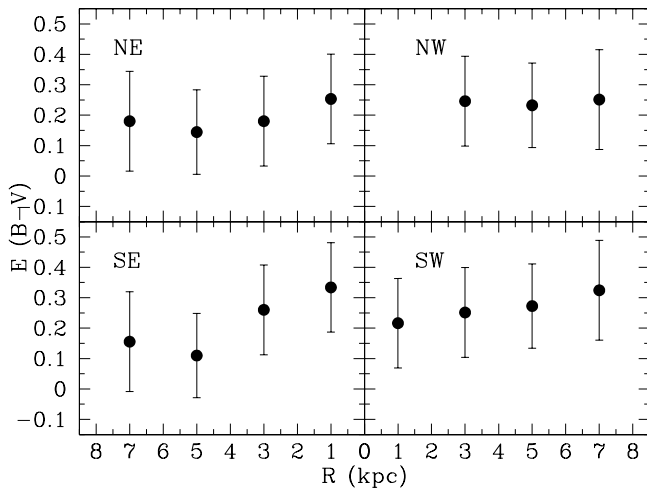


Fig. 3. The radial dependence of the extinction in the four quadrants of M 33: NE north-east, NW north-west, SE south-east, and SW south-west. Note that in the NE and SE quadrants the x axes are inverted to reproduce, together with the other quadrants, the global radial behaviour of the extinction in the galaxy, with the inner regions of the galaxy located in the centre of the plot. The *filled circles* show the mean extinction in each 2 kpc wide bin.

outer zones while the latter in the internal zones. They found a radial dependence of the extinction:

$$A_V = 2.3 - 0.07 \times R \quad (1)$$

where R is the galactocentric distance expressed in arcmin.

Devereux et al. (1997) on the other hand, analyzing a sample of small H II regions, found an average extinction $A_V \sim 1$ mag from radio to $H\alpha$ comparison, with no systematic dependence on radius. They explained their results contrasting those by Israel & Kennicutt (1980) as if the bright H II regions show a radial dependence of extinction while the fainter ones do not. Our data are consistent with the results of Devereux et al. (1997). The absolute value of our average extinction, $A_V=0.65$, based on Balmer

lines ratios and thus involving only the outer parts of the H II regions, is slightly lower, as expected, than the value derived by radio and optical Balmer line comparison, $A_V \sim 1$.

4. Emission-line ratio diagrams

In order to minimize the effect of the reddening correction, we have chosen, when possible, ratios of emission-lines which are close to each other in wavelength: $[O III]\lambda 500.7 \text{ nm}/H\beta$, $[N II]\lambda 658.4 \text{ nm}/H\alpha$, and $[S II]\lambda\lambda 671.7-673.0 \text{ nm}/H\alpha$. The $[N II]$ and $[S II]$ emission lines with respect to $H\alpha$ are useful to separate photoionization and shock-ionization mechanisms, and thus to distinguish among H II regions, PNe and SNRs. In Fig. 4 the observed $[S II]/H\alpha$ and $[N II]/H\alpha$ ratios are plotted. The two dashed lines delineate the limiting values that best separate the photoionized and shock-ionized objects (Galarza et al. 1999). The location of the horizontal dashed line relative to $[N II]/H\alpha$ was shifted to a lower value than indicated by Galarza et al. (1999) for M31 (from $\log([N II]/H\alpha)=-0.3$ to $\log([N II]/H\alpha)=-0.5$) to take into account the lower metallicity of M33.

The vertical line, $[S II]/H\alpha$, was maintained as in M31, since this flux ratio is less sensitive to metallicity. The continuous line marked the lower limit of the PN regions, as derived for a large sample of Galactic PNe by Riesgo & López (2006). The emission-line objects were plotted with different symbols according to their morphology: small isolated regions with high surface brightness (*filled circles*), high surface brightness knots within extended sources (*empty squares*), diffuse and extended objects (*stars*), ring-like nebulae (*empty circles*).

From Fig. 4, we noticed that most of the observed emission-line objects are located in the H II regions area. The correlation of the ratios $[S II]/H\alpha$ and $[N II]/H\alpha$ of H II regions appearing in Fig. 4 is independent of morphological types and depends on the metallicity and excitation of the nebulae, as demonstrated by the photoionization modelling by Viironen et al. (2007). Five of the emission-line objects have ratios consistent with being SNRs. Among them, four have ring-like morphologies, and three of them were indeed already classified as SNRs (see Table 1). Among the candidate PNe present in the literature, one of them, PN CDL04 52, appeared from our LGC images to be a knot of an extended H II region, whereas the position of PN MCM00 66, in the $[S II]/H\alpha$ vs. $[N II]/H\alpha$ diagram is well detached from the area of H II regions and it can be considered a true PN. We excluded then from the following analysis the three known SNRs (M33SNR 15, 25, 64), as well as the two new candidate SNRs LGC-HII 5, BCLMP207a, and the PN MCM00 66.

The radial emission-line ratio distributions presented in Figs. 5, 6, and 7 show a large scatter at each radius, even if some radial trends can be identified. The scatter cannot be attributed to errors in the line fluxes (smaller than the symbols as plotted in Figs. 5 to 7) nor to errors on the position of the nebulae within the galaxy. In fact, the well known inclination ($53^\circ \pm 1^\circ$) of M33 allowed an accurate determination of galactocentric distances. Typical errors on the deprojected galactocentric distances associated with the uncertainty on the inclination were less than 0.1 kpc.

Thus the scatter must be real and represents the fact that each emission-line ratio depends on various characteristics of the nebula, which are not necessarily function of the galactocentric distance (cf. Blair & Long 1997). In particular, it can be ascribed to internal variations in temperature, excitation, and density of the nebula, or to the nature of the ionizing sources, as the relative weight of the O star population which might affect significantly the resulting nebular spectrum.

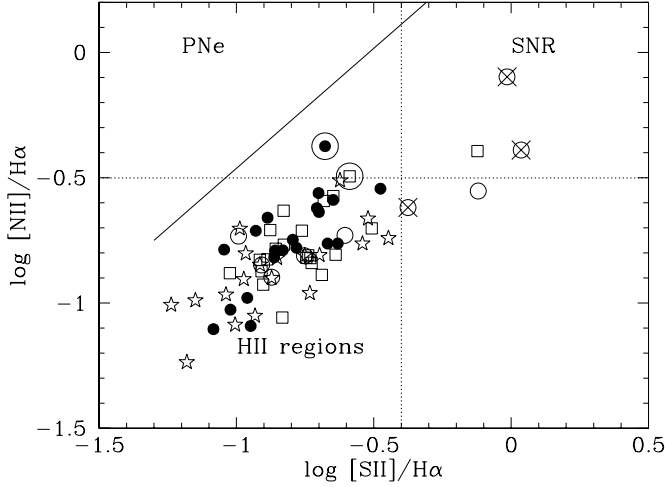


Fig. 4. $[S\ II]/H\alpha$ vs. $[N\ II]/H\alpha$ diagnostic diagram. The different morphological types of emission-line objects are indicated by the following symbols: small isolated (*filled circles*), knots in extended sources (*empty squares*), diffuse and extended objects (*stars*), rings (*empty circles*). The candidate SNRs and PNe known in the literature are marked additionally with further crosses and circles, respectively. Errors on the logarithmic ratios are the order of the size of the symbols. The dashed lines delineate the limiting values that best separate the photoionized and shock-ionized objects (Galarza et al. 1999). Photoionized regions are located in the first quadrant (bottom left). The continuous line marks the lower limit of the PN region, as derived for a large sample of Galactic PNe by Riesgo & López (2006).

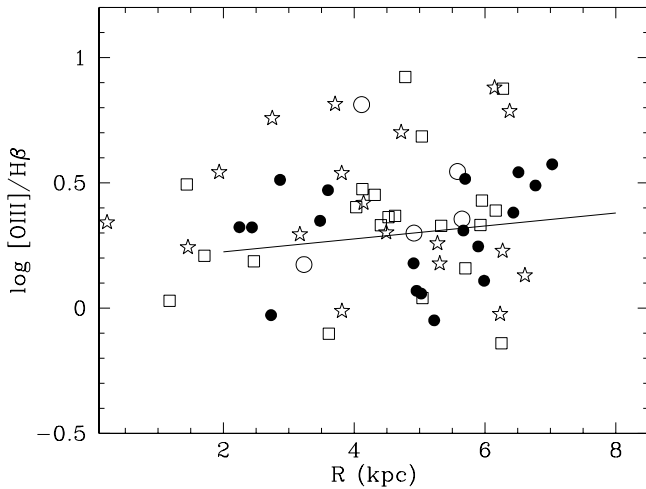


Fig. 5. Radial distribution of $[O\ III]/H\beta$ line ratio in different morphological types of $H\ II$ regions. Symbols and errors as in Fig. 4. The solid line is the fit for the isolated high surface brightness nebulae only (*filled circles*).

Fig. 5 shows the radial variation of $[O\ III]/H\beta$. This ratio measures the excitation of the radiation field within the ionized nebula or, equivalently, the temperature of the central stars. It is also sensitive to chemical composition (Searle 1971). An increase in $[O\ III]/H\beta$ towards the external regions is known to exist in disk galaxies and it is considered to be an evidence for a negative oxygen gradient (Scowen et al. 1992, Zaritsky et al. 1990). However, an empirical correlation between metallicity and the

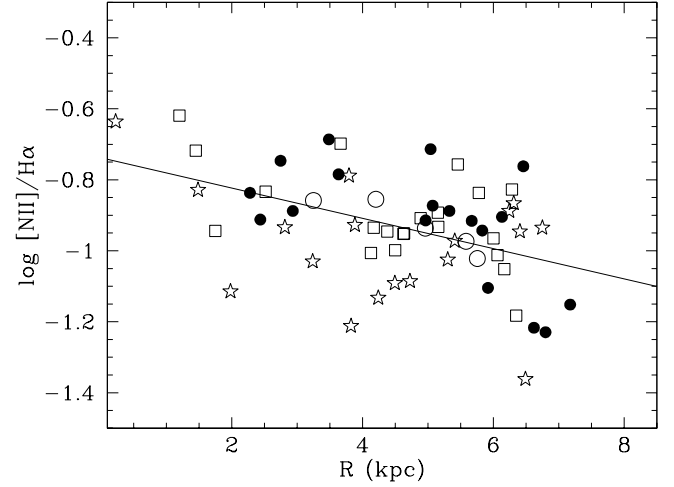


Fig. 6. Radial distribution of $[N\ II]/H\alpha$ line ratio. Symbols and errors as in Fig. 4.

observed $[O\ III]/H\beta$ line ratio cannot be adopted since this line ratio measures only one ionization state of oxygen, O^{2+} , and in low-excitation objects, such as $H\ II$ regions, this might represent a small contribution to the total oxygen abundance. For M33, the expected increase in excitation with galactocentric distance is evident only in small isolated $H\ II$ regions. The diffuse nebulae, including their compact portions, as well as the ring-like nebulae, reproduce only marginally this trend and appear to introduce more scatter in the range covered by the high surface brightness sources, as also observed in M31 $H\ II$ regions (Galarza et al. 1999). The solid line shown in Fig. 5 represents the best-fit to the isolated high surface brightness sources only (*filled circles*).

The radial plot of $[N\ II] 658.4$ relative to $H\alpha$ is shown in Fig. 6. A decreasing trend toward the outer disk of M33 is evident, mainly due to the abundance gradient. In fact, the intensity of $[N\ II]$ lines is not affected by collisional de-excitation, consequently is insensitive to electron density, while it is mostly dependent to the nitrogen abundance (cf. Viironen et al. 2007). Note however that the scatter in the relation is huge, approximately a factor 3 at given radius, rendering this line ratio useful only for a qualitatively detection of the abundance effect on the gradient.

The radial distribution of $[S\ II] 671.7, 673.1$ relative to $H\alpha$ is shown in Fig. 7. There is no clear radial trend, as expected by theoretical modeling by e.g. Domgorgen & Mathis (1994).

5. Physical and chemical properties

5.1. Electron density and temperature

The electron densities, n_e , were measured in almost all the analyzed emission-line objects using the $[S\ II] I(671.7)/I(673.1)$ ratio, which is sensitive to n_e because of the collisional de-excitation of the 671.7 nm transition, but almost insensitive to the electron temperature. We used a five-level atom statistics to compute n_e , assuming the electron temperature as measured from the $(I(500.7)+I(495.9))/I(436.3)$ ratio, when available, and $T_e=10000$ K in the other cases. For four $H\ II$ regions we gave a direct measurement of the electron density and for the remaining ones we gave an upper limit.

Most of our $H\ II$ regions have electron densities or their upper limits consistent with the low density limit for nebulae, i.e.

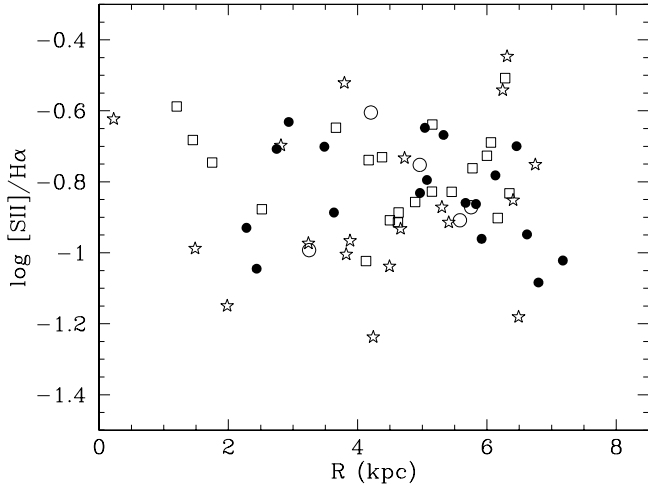


Fig. 7. Radial distribution of $[S \text{ II}]/H\alpha$ line ratio. Symbols and errors as in Fig. 5.

$n_e < 100 \text{ cm}^{-3}$, including the PN candidate (MCM00 66) and the five supernova remnants (SNR M33SNR 15, 25, 64, LGC-HII-5, BCLMP207a) observed in our sample. Only three H II regions have a higher n_e , namely LGC-HII-1, BCLMP 220, and BCLMP 705. Electron density values or their upper limits are listed in Tab. 2.

Electron temperatures, T_e , were derived using the ratio $[O \text{ II}] (I(500.7) + I(495.9))/I(436.3)$ in 15 H II regions. In three of them, where $[N \text{ II}] 575.5 \text{ nm}$ was detectable, we also derived T_e using the ratio $[N \text{ II}] (I(658.4) + I(654.8))/I(575.5)$, finding agreement, within the errors, between $T_{e[N \text{ II}]}$ and $T_{e[O \text{ III}]}$. In addition, an upper limit to T_e was given in other 7 H II regions (see Table 2).

In Fig. 8, the derived $T_{e[O \text{ III}]}$ (filled circles) and $T_{e[N \text{ II}]}$ (empty circles) are plotted versus the deprojected galactocentric distance of the H II regions. The plot shows the presence of a gradient of electron temperatures across the galaxy, with a slope of $570 \pm 130 \text{ K kpc}^{-1}$. This is clearly related to the existence of an abundance gradient, since metal poorer H II regions have a higher electron temperature due to the less effective cooling.

For the H II regions where only $T_{e[O \text{ III}]}$ was measured we adopted the relationships by Izotov et al. (2006) for high Z galaxies, $12 + \log(O/H) > 8.2$, following their definition:

$$T_{e[O \text{ II}]} = 2.967 + T_{e[O \text{ III}]} \times (-4.797 + 2.827T_{e[O \text{ III}]}) \quad (2)$$

and

$$T_{e[S \text{ III}]} = 1.653 + T_{e[O \text{ III}]} \times (-2.261 + 1.605T_{e[O \text{ III}]}) \quad (3)$$

where $T_{e[O \text{ II}]}$, $T_{e[O \text{ III}]}$, and $T_{e[S \text{ III}]}$ are both expressed in 10^4 K unit. Following Izotov et al. (2006), we then adopted $T_{e[O \text{ II}]}$ for the calculation of N^+ , O^+ , S^+ abundances and $T_{e[S \text{ III}]}$ for the calculation S^{2+} and Ar^{2+} abundances, while $T_{e[O \text{ III}]}$ directly measured was used for O^{2+} and He^+ abundances.

5.2. Chemical abundances

The spectral coverage of our observations allows the determination of ionic and total abundances of several elements, namely He/H , N/H , O/H , S/H , and Ar/H . In order to limit the uncertainty due to the use of ionization correction factors (ICFs), we considered only the spectra where both $[O \text{ II}]$ and $[O \text{ III}]$ (including the temperature sensitive line, $[O \text{ III}] 436.3 \text{ nm}$) emission lines are

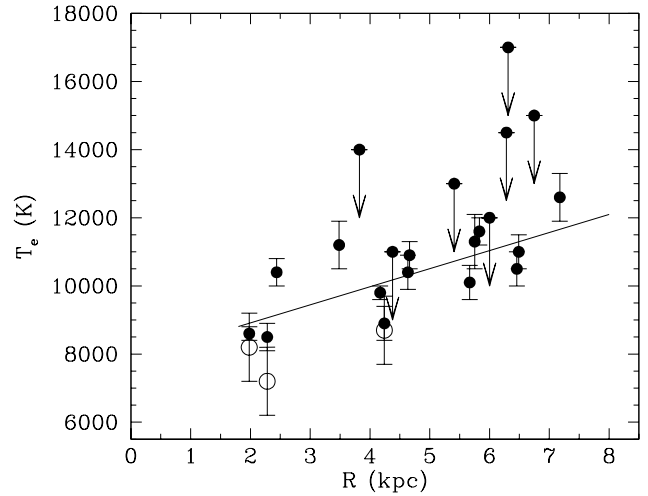


Fig. 8. Electron temperature, T_e , as a function of galactocentric distance: $T_{e[O \text{ III}]}$ (filled circles) and $T_{e[N \text{ II}]}$ (empty circles). Upper limits to the $T_{e[O \text{ III}]}$ are marked with an arrow. The solid line is the weighted linear least-squares fit to the $T_{e[O \text{ III}]}$ values (excluding the upper limits).

measured with sufficient accuracy ($S/N > 3$). In fact, H II regions are generally low-excitation objects and a relevant percentage of their oxygen is only once ionized. Consequently $[O \text{ II}]$ emission lines are very relevant in the calculation of the total oxygen abundance. In addition, the ICFs used to compute the total abundance of the other chemical elements are all expressed as a function of both oxygen ionization stages, either $O^+/(O^+ + O^{2+})$ or $O^{2+}/(O^+ + O^{2+})$. We used $He \text{ I } \lambda 587.6 \text{ nm}$ and $He \text{ II } \lambda 468.6 \text{ nm}$ for the determination of the helium abundance, $[N \text{ II}] \lambda\lambda 654.8, 658.4 \text{ nm}$ for the nitrogen abundance, $[O \text{ II}] \lambda\lambda 732.0, 733.0 \text{ nm}$ and $[O \text{ III}] \lambda\lambda 495.9, 500.7 \text{ nm}$ for the oxygen abundance, $[S \text{ II}] \lambda\lambda 671.7, 673.1 \text{ nm}$ and $[S \text{ III}] \lambda 631.2 \text{ nm}$ for the sulfur abundance, and $[Ar \text{ III}] \lambda 713.5 \text{ nm}$ for the argon abundance.

Ionic O^+ abundances are usually computed from the $[O \text{ II}] \lambda\lambda 372.7, 372.9 \text{ nm}$ line fluxes. However, the $[O \text{ II}] \lambda\lambda 732.0, 733.0 \text{ nm}$ lines should be used when, as in our case, the brighter emission lines $\lambda\lambda 372.7, 372.9 \text{ nm}$ are not available (c.f. Izotov et al. 2006). A comparison of O^+ abundances derived from both sets of lines in a sample of about 200 SDSS H II galaxies is presented by Kniazev et al. (2004). They found a weighted mean of the differences between the two sets of abundances $\log(O/H)_{372.7,372.9} - \log(O/H)_{732.0,733.0} = 0.002 \pm 0.002 \text{ dex}$, with a rms scatter of 0.02 dex in both cases, and conclude that this scatter is within the uncertainties as expected from Aller (1984). However, it has to be noted that the intrinsic weakness of $[O \text{ II}] 732.0, 733.0 \text{ nm}$ lines, with respect to the $[O \text{ II}] 372.7, 372.9 \text{ nm}$, produces larger errors in the abundance determination.

We adopted the prescriptions by Izotov et al. (1994) to derive the helium ionic abundances, and by Izotov et al. (2006) to derive the oxygen, nitrogen, sulfur, and argon ionic abundances and ICFs. Uncertainties on the ionic and total abundance were computed with a standard propagation of the errors on the flux measurements, which propagates to the de-reddening procedure, to the electron temperature and density derivations, and to the ICFs computation. The ionic and total abundances with their errors are reported in Table 3.

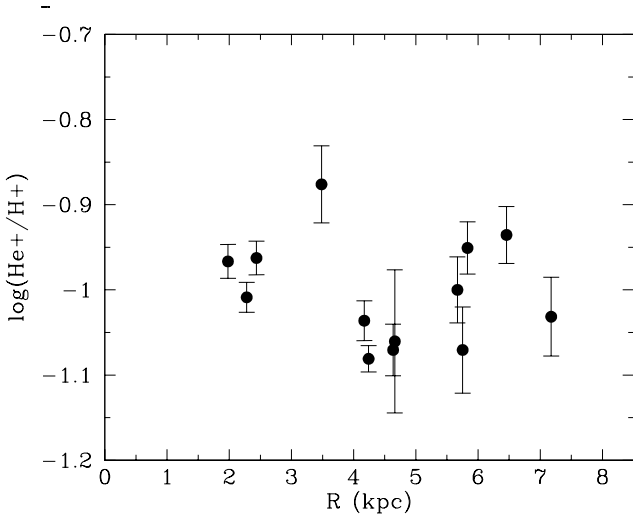


Fig. 9. The He⁺/H⁺ abundance versus galactocentric distance.

6. The metallicity gradients in M 33

6.1. Helium

In Fig. 9 we present the determinations of the ionic He⁺/H⁺ abundance as a function of galactocentric distance. There is no clear indication of radial gradient. While the range of the He⁺/H⁺ abundance found here appears consistent with previous works, the correction for neutral helium is very uncertain and therefore the helium abundance gradient is difficult to derive. Nonetheless, assuming the ICF scheme of He based on the η parameter (e.g. Pagel et al. 1992; Vílchez et al. 1988), we can put a limit for those H II regions at radii lower than 3 kpc for which a value of η can be derived; for these H II regions an ionization correction factor, ICF(He) > 1.2 is suggested by our observations. Further observations are needed to confirm these claims.

6.2. Oxygen

In Fig. 10, we show the oxygen abundance as a function of galactocentric distance for the 14 H II where we measured the chemical abundances. A weighted linear least-square fit to our data (solid line) gives a gradient:

$$12 + \log O/H = -0.054(\pm 0.011) \times R + 8.53(\pm 0.05). \quad (4)$$

where R is the deprojected galactocentric distance in kpc, computed assuming a distance of 840 kpc, an inclination of 53°, and a parallactic angle of 22°.

The figure also shows the oxygen abundances, re-derived using the Izotov's et al. (2006) ionic abundance and ICF formulae, from all previous spectroscopic observations which allowed a direct determination of the electronic temperature (Kwitter & Aller 1981, Vílchez et al. 1988, and Crockett et al. 2006, as shown in Table 4). In case of multiple measurements of the same H II region we have adopted spectroscopic data from the most recent observations. Where both [O II] 372.7 and 732.5 emission lines were available from the literature (four H II regions), we recomputed the ionic O⁺ with both set of lines. The agreement is very good, as shown in Table 4. Considering the whole sample of oxygen measurements, the gradient still has a slope of ~ -0.06 dex kpc⁻¹, consistent with our determination and with gradients measured in other non-barred galaxies of similar morphological type (e.g. NGC 2403, Garnett et al. 1997).

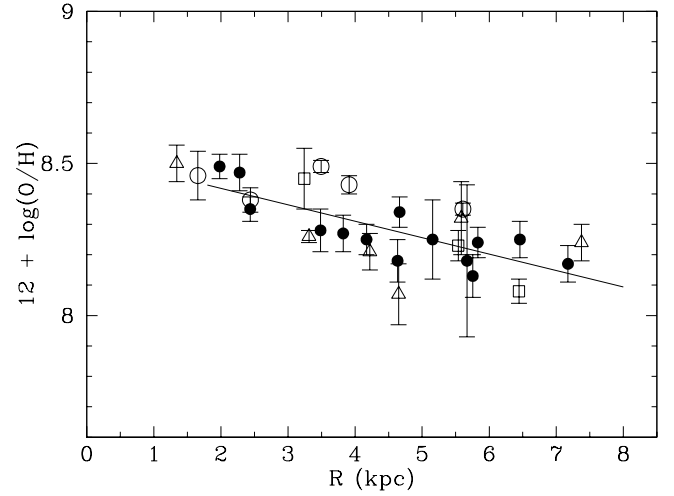


Fig. 10. The O/H abundance (with electron temperature derived from observations) versus the galactocentric distance: *filled circles* from the present work, *empty squares* from Kwitter & Aller (1981), *empty circles* from Vílchez et al. (1988), and *triangles* from Crockett et al. (2006). The solid line is the weighted linear least-squares fit to our 14 H II regions.

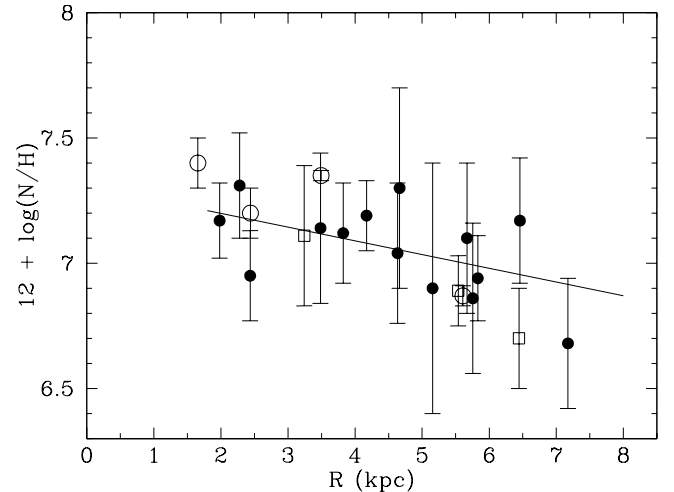


Fig. 11. The 12+log(N/H) abundance vs. galactocentric distance (symbols and line types as in Fig. 10).

6.3. Nitrogen

In Fig. 11 the radial variation of the nitrogen abundance is shown. A weighted linear fit of our data gives a gradient

$$12 + \log N/H = -0.06(\pm 0.02) \times R + 7.3(\pm 0.1) \quad (5)$$

similar to the oxygen one. If also previous determinations are considered, the overall slope of the gradient, results to be a bit steeper, namely ~ -0.10 dex kpc⁻¹.

In Fig 12, we present the relationship of N/O and the oxygen abundance. It appears that in M33 the N/O ratio is constant within errors, with a value around $\log(N/O) = -1.2$, in between solar (-0.9 , Asplund et al. 2005) and the value for dwarf irregular galaxies ($\log(N/O) = -1.5$). This probes that N/O along galactic disks does not always follow the relation N/O proportional to O/H, as expected for a purely secondary enrichment behaviour. The almost constant value of N/O with respect to O/H in M33

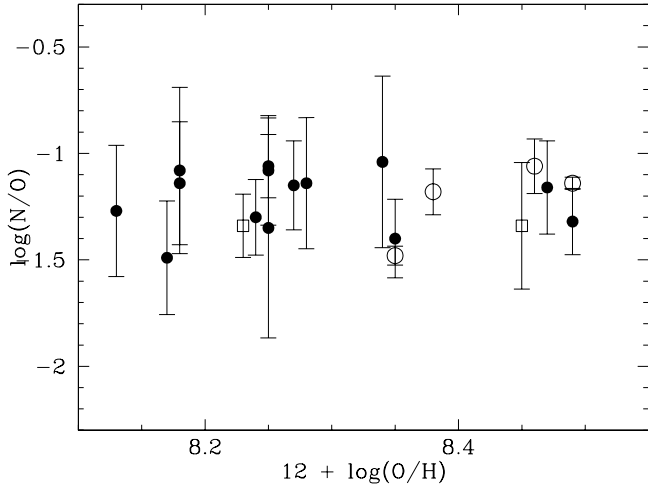


Fig. 12. $\log N/O$ vs. $12 + \log(O/H)$ (symbols and line types as in Fig. 10).

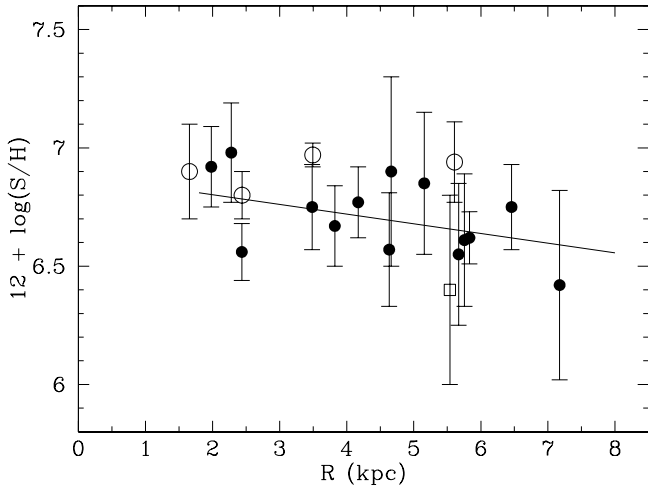


Fig. 13. The $12 + \log(S/H)$ abundance vs. galactocentric distance (symbols and line types as in Fig. 10).

warns us against the use of abundance determination which are based on models assuming that the N/O ratio is proportional to O/H , and then using $[N\text{ II}]/[O\text{ II}]$ to infer the metallicity. M33 shows that at least in some galaxy disks this is not true.

6.4. Sulfur

Our spectral range did not allow the observation of the infrared $[S\text{ III}]$ emission lines, but the auroral line $[S\text{ III}]$ 631.2 nm and $[S\text{ II}]$ 671.7, 673.0 nm were observed in a large number of $H\text{ II}$ regions of our sample. This allowed us to measure the total sulfur abundance, since the larger amount of sulfur is in the form of S^+ and S^{2+} , while the other ions S^{3+} and S^{4+} contribute less. The total S/H was however computed taking also into account of the correction for the unseen ionization stages, mainly S^{3+} , using the $ICF(S)$ by Izotov et al. (2006). On the other hand, errors on the total sulfur abundance measured via the $[S\text{ III}]$ 631.2 nm and $[S\text{ II}]$ 671.7, 673.0 nm lines are larger than via IR lines, since these emission lines are generally weaker. Typical errors, in the range 0.1-0.4 dex, are indicated in Table 3. The gradient of sulfur, as expected, resembles that of oxygen, since these elements

are both produced in stars belonging to the same mass range ($M > 10 M_{\odot}$). A weighted linear fit of our data gives

$$12 + \log S/H = -0.04(\pm 0.02) \times R + 6.88(\pm 0.11). \quad (6)$$

7. Discussion

The wealth of information collected during the last twenty years on the metallicity distribution in the interstellar medium and young stars of M33 allowed us to draw a general picture of its present time gradient.

Individual studies, with small samples of objects, would lead to significantly different - and thus uncertain - conclusions. In fact, in contrast with the result by Garnett et al. 1997, indicating a mean gradient through the whole disk of M33 of -0.11 dex kpc^{-1} , more recent studies suggest a shallower metallicity gradient derived for Ne and O. Since both elements are produced mainly by short-lived, massive stars ($M > 10 M_{\odot}$), the slope of their gradient should be very similar. In our Galaxy and in nearby galaxies, the abundances of these two elements are generally closely correlated, as supported by abundance measurements in Galactic and extragalactic PNe (Henry 1990), showing that Ne/O is in a good approximation constant over a wide range of O/H values. This constancy of oxygen and neon is, however, in apparent contrast with the results obtained by Willner & Nelson-Patel (2002), who derived Ne abundances for 25 $H\text{ II}$ regions in M33 from infrared spectroscopy. The best fit to the complete sample of their data is a step function in a diagram showing the abundance of neon (relative to the solar one) versus the galactocentric distance: -0.15 dex from 0.7 to 4 kpc, and -0.35 from 4 to 6.7 kpc. Avoiding the two outermost $H\text{ II}$ regions of their sample they found a best-fit slope -0.05 ± 0.02 dex kpc^{-1} . An even shallower slope for the Ne/H gradient was found by Crockett et al. (2006), -0.016 dex kpc^{-1} .

In order to avoid peculiarity effects due to the limited size of different samples, we have considered, in addition to the present work results, oxygen measurements in a large number of objects representative of the present time ISM metallicity: $H\text{ II}$ regions (optical spectroscopy² by Kwitter & Aller 1981, Vílchez et al. 1988, Crockett et al. 2006, and infrared spectroscopy³ by Willner & Nelson-Patel 2002) and young stars (Monteverde et al. 1997, Urbaneja et al. 2005, Beaulieu et al. 2006). The abundances were averaged in bins 1 kpc wide, starting from the center of the galaxy. The errors are the *rms* scatter of the average value in each bin.

From Fig. 14, it is clear the oxygen gradient cannot be fitted with a single slope, that would exclude the inner points with higher metallicity. Two different slopes in the central and outer regions are needed instead. The best fit gives for the region from the center to 3 kpc

$$12 + \log O/H = -0.19(\pm 0.08) \times R + 8.95(\pm 0.13) \quad (7)$$

and for the radial region from 3 to 8 kpc

$$12 + \log O/H = -0.038(\pm 0.015) \times R + 8.49(\pm 0.08). \quad (8)$$

The existing conflict on the determination of the slope of the M33 metallicity gradient might be solved using the result of

² for these $H\text{ II}$ regions we have re-computed uniformly chemical abundances using the Izotov's et al. (2006) ionic abundance and ICF formulae, only for the $H\text{ II}$ regions where the electron temperature diagnostic lines were available (see Table 4)

³ Neon abundance were converted into oxygen using the solar ratio O/Ne by Asplund et al. (2005)

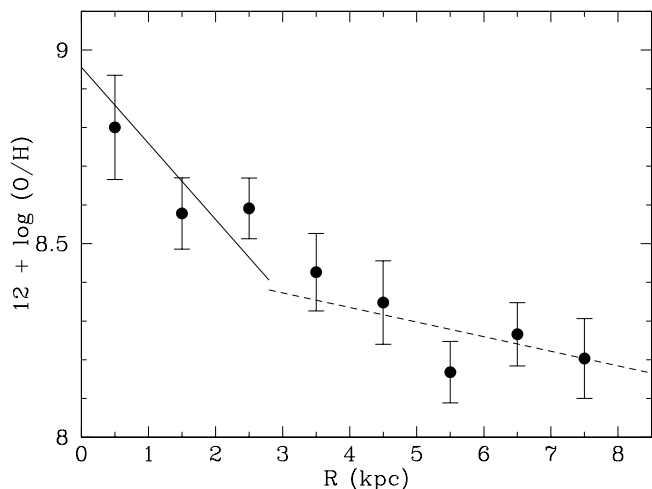


Fig. 14. Mean oxygen abundance from H II regions and young stars as indicated in the text vs. galactocentric distance. The best-fit is a linear fit with two slopes: -0.19 ± 0.08 dex kpc^{-1} for $R < 3$ kpc (solid line) and -0.038 ± 0.015 dex kpc^{-1} (dashed line) for $R \geq 3$ kpc.

Fig. 14, which involves all the best chemical abundance determinations in this galaxy, including nebular abundances with direct T_e measurement and stellar abundances. Stasinska et al. (2006) discussed the reliability of chemical abundance derived in high metallicity H II regions: even if the [O III] 436.3 line is measured, the derived O/H might be anyhow underestimated since strong temperature gradients inside the nebula due to the cooling by [O III] 52, 88 μm make the [O III] 436.3/500.7 ratio overestimate the temperature. Nonetheless this effect discussed is expected to be significant only for abundances larger than the solar value, in the case of M 33 this refers possibly to the central kpc. Thus the presence of stellar abundances, which are not affected by the same problems of nebular abundances in the high metallicity regime, makes the result of Fig. 14 more robust.

Since the gradient in M 33 cannot be represented by a single linear fit, studies undertaken in different radial regions would produce extremely different results: if inner regions were included, a steeper gradient would result. On the contrary if only regions far from the center were considered, a flatter gradient would be obtained. We remind that the steepening of the inner gradient is also sustained by individual studies (e.g. Vílchez et al. 1988, Beaulieu et al. 2006). Moreover, the relatively shallow slope of the outer metallicity gradient is confirmed by several recent works, as the previously quoted papers by Willner & Nelson-Patel (2002), Urbaneja et al. (2005), Crockett et al. (2006). Also recent works are obtaining noteworthy results, as the work by Viironen et al. (2007) and that by Rosolowsky & Simon (2006). The former is studying via photoionization modelling the dependence on metallicity of location of H II regions in the diagnostic diagram [N II]/H α vs [S II]/H α . For M33, using the sample of H II regions presented in this work and data of literature, they found a gradient across all the disk of -0.05 ± 0.01 dex kpc^{-1} . The latter work, called “M33 Metallicity Project”, is studying a large number of H II regions in a South-West region of M33 via optical spectroscopy. They measure an oxygen abundance gradient of -0.03 dex kpc^{-1} .

From a theoretical point of view, Magrini et al. (2007) present in an accompanying paper a detailed model of the chemical evolution of the disk of M 33. The model is able to reproduce

the observed gradients, together with other observables, as the gas and star distribution, and the star formation rate. The predicted oxygen abundance gradient is -0.067 dex kpc^{-1} , across the whole disk excluding the inner 1 kpc regions⁴ in excellent agreement with the best fit to the data in Fig. 14 in the same radial region, -0.07 ± 0.01 dex kpc^{-1} .

The relatively shallow slope and the apparent flattening with time of the gradient obtained from the comparison of the present time gradient with PN (Magrini et al. 2004) and RGB stars (Barker et al. 2006) gradients, are explained by the model with a slow continuous formation of the disk by infall. A conspicuous cloud of neutral gas infalling into the disk of M33 recently detected at 21-cm by Westmeier et al. (2005) and the presence of carbon stars found at larger radii where the drop of the H α flux occurs (Davidge 2003, Block et al. 2004, 2006, Rowe et al. 2005) support this picture, suggesting that accretion of gas in the disk of M 33 is still taking place.

The results of this model and the new detailed observations available for M 33 open new scenarios on the formation of spiral galaxies. These scenarios are not in opposition to the “classical” models of galactic disk formation, i.e. rapid collapse of an initial halo, but they extend them with the possibility of further frequent accretion events from mergers and interactions in the intergalactic medium. A full discussion of chemical evolution modeling for M 33 is given by Magrini et al. (2007).

8. Conclusions

We analyzed optical spectra of 72 emission-line objects in M 33, including mostly H II regions, but also five SNRs and two candidate PNe. Most of the emission-line objects are in the low density limit, with $n_e < 100$ cm^{-3} , only three of them have higher density. The direct T_e determination was possible for 15 H II regions by the measurements of the [O III] 436.3 nm line and in three of them of the [N II] 575.5 nm line.

The radial variation of several emission-line ratios does not appear to be much affected by the different morphology of the H II regions, even if in the [O III]/H β diagram the higher surface brightness sources show a higher correlation, signature of spectra dominated by local chemical abundance effects. Emission-line ratio diagrams allowed us to separate the different types of emission-line objects and to infer the presence of metallicity gradients.

For the 14 H II regions with determined T_e and with detection of both [O II] and [O III] lines we derived chemical abundances using the ICF methods. We found metallicity gradients in good agreement with previous determinations in the same radial regions. The resulting global oxygen abundance gradient is -0.06 ± 0.01 dex kpc^{-1} .

We collected oxygen measurements in a large number of objects representative of the present time ISM metallicity to draw a complete picture of the shape and magnitude of the metallicity gradient. We found the best fit to the data using two different slopes, corresponding to the central regions $R < 3$ kpc (-0.19 ± 0.08 dex kpc^{-1}) and outer regions $R \geq 3$ kpc (-0.038 ± 0.015 dex kpc^{-1}). The shallower outer gradient is in agreement with several new works and it can be explained with a slow continuous accretion of the disk of M 33 from the intergalactic medium.

Acknowledgements. R.L.M.C., A.M., and P.L. acknowledge financial support from the Spanish Ministry of Science and Education (grant AYA02-00883). The

⁴ The model does not take into account the central bulge and thus cannot reproduce the central enhancement of the metallicity.

work of L.M. is supported by a INAF post-doctoral grant 2005. We are grateful to Edvige Corbelli for many useful discussions about M33, and for suggestions about the radial behaviour of the extinction.

References

- Aller, L. H. 1942, ApJ, 95, 52
 Aller, H. L. 1984, Physics of Thermal Gaseous Nebulae (Dordrecht: Reidel)
 Asplund, M., Grevesse, N., Sauval, A. J. 2005, ASPC, 336, 25
 Barker, M. K., Sarajedini, A., Geisler, D., Harding, P., Schommer, R. 2006, AJin press, astro-ph/0611892
 Beaulieu, J.-P., Buchler, J. R., Marquette, J.-B., Hartman, J. D., Schwarzenberg-Czerny, A., 2006, ApJ, 653, 101
 Blair, W. P., Long, K. S., 1997, ApJS, 108, 261
 Block, D. L., Freeman, K. C., Jarrett, T. H., Puerari, I., Worthey, G., Combes, F., Gross, R. 2004, A&A, 425, 37
 Block, D. L., Puerari, I., Stockton, A. et al. 2006, IAUS, 235, 8
 Boulesteix, J., Courtes, G., Laval, A., Monnet, G., Petit, H., 1974, A&A, 37, 33
 Brooks, R. S., Wilson, C. D., Harris, W. E. 2004, AJ, 128, 237
 Calzetti, D., Kinney, A. L., Ford, H., Doggett, J., Long, K. S. 1995, AJ, 110, 2739
 Cardwell, A., Beckman, J. E., Magrini, L., Zurita, A. 2000, in The interstellar medium in M31 and M33. Proceedings 232, Eds by E. M. Berkhuijsen, R. Beck, and R. A. M. Walterbos. S. Aachen, 115
 Chieffi, A., Limongi, M. 2004, ApJ, 608, 405
 Ciardullo, R., Durrell, P. R., Laychak, M. B., Herrmann, K. A., Moody, K., Jacoby, G. H., Feldmeier, J. J., 2004, ApJ, 614, 167
 Corradi, R. L. M., Magrini, L., 2006, in Planetary Nebulae Beyond the Milky Way, ESO Astrophysics Symposia, 36
 Courtes, G., Petit, H., Petit, M., Sivan, J.-P., Dodonov, S. 1987, A&A, 174, 28
 Crockett, N. R., Garnett, D. R., Massey, P., Jacoby, G. 2006, ApJ, 637, 741
 Davidge, T. J. 2003, AJ, 125, 304
 Devereux, N., Duric, N., Scowen, P. A., 1997, AJ, 113, 236
 Domgorgen, H., Mathis, J. S., 1994, ApJ, 428, 647
 Filippenko, A. V. 1982, PASP, 94, 715
 Freedman, W. L., Wilson, C. D., Madore, B. F. 1991, ApJ, 372, 455
 Galarza, V., Walterbos, R. A. M., Braun, R., 1999, AJ, 118, 2775
 Galletti, S., Bellazzini, M., Ferraro, F., 2004, A&A, 423, 925
 Garnett, D. R., Shields, G. A., Skillman, E. D., Sagan, S. P., Dufour, R. J. 1997, ApJ, 489, 63
 Gordon, S. M., Duric, N., Kirchner, R.P., Goss, W.M., Viallefond, F., 1999, ApJS, 120, 247
 Henry, R. B. C. 1990, ApJ, 356, 229
 Henry, R. B. C., Worthey, G., 1999, PASP, 111, 919
 Herrero, A., Lennon, D. J., Vílchez, J. M., Kudritzki, R. P., Humphreys, R. H. 1994, A&A, 287, 885
 Hirschi, R., Meynet, G., Maeder, A. 2005 Nuclear Physics A, 758, 234
 Hodge, P. W., Balsley, J., Wyder, T. K., Skelton, B. P., 1999, PASP, 111, 685
 Hodge, P. W., Skelton, B. P., Ashizawa, J., 2002, An Atlas of Local Group Galaxies, Astrophysics and Space Science Library, Volume 221. Kluwer Academic Publishers, Dordrecht
 Holmberg, E., 1958, Lund Medd. Astron. Obs. Ser. II, 136, 1
 Israel, F. P., Kennicutt, R. C., 1980, ApJ, 21, 1
 Izotov, Y.I., Thuan, T. X., Lipovetsky, V. A., 1994, ApJ, 435, 647
 Izotov, Y.I., Stasinska, G., Meynet, G., Guseva, N. G., Thuan, T. X., 2006, A&A, 448, 955
 Kennicutt, R. C., Jr., Garnett, D. R., 1996, ApJ, 456, 504
 Kim, M., Kim, E., Lee, M. G., Sarajedini, A., Geisler, D. 2002, AJ, 123, 244
 Kniazev, A., Pustilnik, S.A., Grebel, E. K., Lee, H., Pramskij, A.J., ApJS, 153, 429
 Kwitter, K. B., Aller, L. H., 1981 MNRAS, 195, 939
 Magrini, L., Corradi, R. L. M., Mampaso, A., Perinotto, M. 2000, A&A, 355, 713
 Magrini, L., Perinotto, M., Corradi, R. L. M., Mampaso, A. 2003, A&A, 400, 511
 Magrini, L., Perinotto, M., Mampaso, A., Corradi, R. L. M. 2004, A&A, 426, 779
 Magrini, L., Corbelli, E., Galli, D. 2007, A&A, submitted
 Magrini, L., Perinotto, M., Mampaso, A., Corradi, R. L. M. 2004, A&A, 426, 779
 Mathis, J. S., 1990, ARA&A, 28, 37
 McCarthy, J. K., Lennon, D. J., Venn, K. A., Kudritzki, R.-P. 1995, ApJ, 455, 135
 Monteverde, M. I., Herrero, A., Lennon, D. J., Kudritzki, R.-P. 1997, ApJ, 474, 107
 Monteverde, M. I., Herrero, A., Lennon, D. J. 2000, ApJ, 545, 813
 Oke, J. B., 1990, AJ, 99, 1621
 Pagel, B. E. J., Simonson, E. A., Terlevich, R. J., Edmunds, M. G. 1992, MNRAS, 255, 325
 Pérez-Montero, E., Díaz, I. A., 2005, MNRAS, 361, 1063
 Pilyugin, L. S., 2001, A&A, 369, 594
 Riesgo, H., López, J. A., RMxAA, 42, 47
 Rosolowsky, E., Simon, J. D., 2006, AAS, 209, 5507
 Rowe, J. F., Richer, H. B., Brewer, J. P., Crabtree, D. R. 2005, AJ, 129, 729
 Scowen, P. A., Dufour, R. J., Hester, J. J., 1992, AJ, 104, 92
 Searle, L., 1971, ApJ, 168, 327
 Smith, H. E. 1975, ApJ, 199, 591
 Stasinska, G., Vílchez, J. M., Perez, E., Gonzalez Delgado, R. M., Corradi, R. L. M., Mampaso, A., Magrini, L., 2006, in Planetary Nebulae Beyond the Milky Way, ESO ASTROPHYSICS SYMPOSIA, Springer, p. 234
 Stephens, A. W., Frogel, J. A. 2002 AJ, 124, 2023
 Tiede, G. P., Sarajedini, A., Barker, M. K. 2004 AJ, 128, 224
 Tosi, M., 1988, A&A, 197, 47
 Urbaneja, M. A., Herrero, A., Kudritzki, R.-P., Najarro, F., Smartt, S. J., Puls, J., Lennon, D. J., Corral, L. J. 2005, ApJ, 635, 311
 van den Bergh, S., 2000 in *The Galaxies of the Local Group*, Cambridge University Press
 Venn, K. A., McCarthy, J. K., Lennon, D. J., Kudritzki, R. P. 1998 ASPC, 147, 54
 Viallefond, F., Goss, W. M., Van der Hulst, J.M., Crane P.C., 1986, ApJS, 64, 237
 Viironen, K., Delgado-Iñiesta, G., Mampaso, A., Magrini, L., Corradi, R. L. M., 2007, MNRAS, submitted
 Vílchez, J. M., Pagel, B. E. J., Diaz, A. I., Terlevich, E., Edmunds, M. G., 1988 MNRAS, 235, 633
 Vílchez, J. M., Esteban, C. 1996, MNRAS, 280, 720
 Westmeier, T., Braun, R., Thilker, D. 2005, A&A, 436, 101
 Willner, S. P., Nelson-Patel, K. 2002, ApJ, 598, 679
 Wyder, T. K., Hodge, P. W., Skelton, B. P. 1997, PASP, 109, 927
 Zaritsky, D., Hill, J. M., Elston, R., 1990, AJ, 99, 1108

Table 1. The list of emission line objects spectroscopically observed in M 33, including H II regions, SNRs and PNe. The identification names are from: BCLMP– Boulesteix et al. (1974); CPSDP– Courtes et al. (1987); VGVC– Viallefond et al. (1986); GDK99– Gordon et al. (1996); MCM00– Magrini et al. (2000); CDL04– Ciardullo et al. (2004). The emission-line objects not identified in previous works, mostly small isolated H II regions, are labeled with LGC-HII-n, standing for H II regions discovered by the Local Group Census project (cf. Corradi & Magrini 2006). The coordinates J2000.0 of the position of the fibers projected on the sky are shown in the second and third columns. They do not correspond exactly to the center of the emission line objects, but generally to the maximum [O III] emissivity. The observed photometric fluxes in unit of 10^{-15} erg/cm², $F_{H\alpha}$, and the area in arcsec² were taken from Hodge et al. (2002), when this information is available, otherwise their were measured in the LGC INT images (columns 4th, 5th). The last column shows the main characteristic of the morphology: *e* extended, *c* small/isolated, *k* high surface brightness knot in an extended complex, *s* shell/ring-like.

Id	Name	RA	Dec	$F_{H\alpha}$ (10^{-15} erg/cm ² s)	Area (arcsec ²)	Morphology
		J2000.0				
3	BCLMP 275a	1:32:29.5	30:36:08	80	187	e
4	LGC-HII-1	1:32:30.2	30:32:35	15	150	c
7	BCLMP 272	1:32:33.4	30:27:45	520	606	e
8	BCLMP 273b	1:32:33.5	30:30:43	77	207	e
14	BCLMP 266	1:32:40.8	30:24:25	270	497	k
17	BCLMP 263a	1:32:41.8	30:21:17	20	92	k
19	LGC-HII-2	1:32:43.0	30:19:31	20	13	c
22	BCLMP 238	1:32:44.5	30:34:54	270	317	e
26	LGC-HII-3	1:32:45.9	30:41:35	26	28	c
40	BCLMP 240a	1:32:56.8	30:32:16	130	166	k
42	BCLMP 289	1:32:58.5	30:44:29	72	172	k
45	BCLMP 218	1:33:00.3	30:30:47	2400	2684	k
53	M33SNR 15–BCLMP 84	1:33:03.9	30:39:54	96	144	s
56	BCLMP 258b	1:33:06.2	30:23:27	230	340	e
58	BCLMP 288a	1:33:07.3	30:42:35	470	824	k
72	CPSDP 97	1:33:10.6	30:48:23	21	90	k,e
73	MCM00 Em 24	1:33:10.8	30:18:08	3	28	c
75	BCLMP 220	1:33:11.1	30:27:34	550	481	e
76	CPSDP 194	1:33:11.2	30:45:16	500	1466	e
85	BCLMP 256c	1:33:12.2	30:23:29	30	103	e
86	VGHC 2-22	1:33:12.4	30:38:38	420	1500	e
92	BCLMP 618b	1:33:13.3	30:50:32	15	35	k
107	CPSDP 103	1:33:15.4	30:51:59	22	40	c
109	BCLMP 638N	1:33:15.6	30:56:53	-	-	e
114	BCLMP 626	1:33:16.4	30:54:05	470	617	s
118	CPSDP 107	1:33:19.0	30:58:14	10	78	c
122	LGC-HII-4	1:33:21.2	30:17:54	60	315	s
127	M33SNR 25	1:33:23.9	30:26:15	10	150	s
133	BCLMP 45	1:33:29.0	30:40:25	1400	877	e
157	BCLMP 207a	1:33:35.1	30:29:56	21	57	k
158	BCLMP 640	1:33:35.1	31:00:29	2	600	k,s
165	BCLMP 55b	1:33:36.0	30:42:33	63	229	k
168	CDL04 52-PN	1:33:36.3	30:38:48	7	28	c
186	LGC-HII-5	1:33:40.5	30:10:46	1	28	s
205	CPSDP 221	1:33:46.3	30:52:15	9.9	58	c
207	LGC-HII-6	1:33:47.0	30:27:23	200	78	s
223	BCLMP 637	1:33:50.6	30:56:33	10	1000	e
224	MCM00 PN 66	1:33:50.7	30:37:06	13	28	c
226	BCLMP 93a	1:33:52.6	30:39:08	420	478	e
227	BCLMP 301h	1:33:52.6	30:45:03	120	455	k
236	BCLMP 759	1:33:56.8	30:22:16	37	360	s
249	BCLMP 4a	1:33:59.5	30:35:47	880	494	e
252	GDK99 128	1:33:59.9	30:32:44	200	50	c,k
253	M33-SNR 64	1:34:00.1	30:42:19	3	430	s
259	CPSDP 316	1:34:01.7	30:23:01	15	13	c
271	BCLMP 670	1:34:03.3	30:53:09	10	32	c
276	LGC-HII-7	1:34:04.3	31:02:18	30	192	c
278	VGHC 2-84	1:34:06.7	30:48:56	200	78	c
287	BCLMP 709b	1:34:09.4	30:34:17	45	115	k
289	CPSDP 323	1:34:09.6	30:21:23	17	240	k
311	CPSDP 325	1:34:14.4	30:27:40	1.4	7	c
331	BCLMP 721	1:34:21.3	30:38:00	98	283	e
334	BCLMP 682c	1:34:22.0	30:47:10	79	265	k
337	BCLMP 715b	1:34:23.3	30:33:13	180	493	e
338	CPSDP 189	1:34:23.5	30:31:19	4	21	s
339	BCLMP 659	1:34:24.0	30:57:04	150	224	k
341	LGC-HII-8	1:34:24.3	30:39:07	7	190	c
358	BCLMP 680	1:34:36.1	30:46:00	15	75	k
360	LGC-HII-9	1:34:36.8	30:58:19	2	13	c
363	BCLMP 717b	1:34:37.4	30:34:54	110	147	k
364	LGC-HII-10	1:34:38.5	30:32:52	12	7	c
365	BCLMP 749	1:34:38.9	30:43:58	170	1800	e
367	BCLMP 649	1:34:39.3	31:02:25	50	190	k
369	BCLMP 705	1:34:39.5	30:31:14	110	95	k
377	LGC-HII-11	1:34:42.2	30:24:00	10	50	c
379	MCM00 Em 59	1:34:42.5	30:55:44	26	26	c
383	BCLMP 757	1:34:45.5	30:42:24	30	240	k
387	BCLMP 657	1:34:49.8	30:54:47	25	1800	e
391	LGC-HII-12	1:34:55.1	30:34:51	13	15	c
394	BCLMP 754	1:35:01.6	30:40:02	12	25	k
395	LGC-HII-13	1:35:02.4	31:00:43	26	75	c
398	BCLMP 756	1:35:07.2	30:41:43	50	3000	e

Table 2. Observed line fluxes F_λ of seventy-two emission-line objects, including mainly H II regions (see Tab.1). F_λ are represented on a scale where $F(\text{H}\beta)=100.0$. ‘<’ indicates upper limits. Associated errors are described in the text. Some nebular quantities are also reported: the extinction coefficient, $c(\text{H}\beta)$, the electron density, n_e and the electron temperatures, $T_e([\text{O III}])$ and $T_e([\text{N II}])$

	BCLMP275a	LGC HII 1	BCLMP272	BCLMP273a	BCLMP266	BCLMP263a	LGC HII 2	BCLMP238	LGC HII 3	BCLMP240a
$c(\text{H}\beta)$	0.06±0.02	0.40±0.08	0.30±0.02	0.40±0.04	0.37±0.01	0.08±0.02	0.00±0.01	0.00±0.01	0.27±0.01	0.04±0.02
$T_e([\text{O III}])$ (K)	<15000	-	<17000	-	<12000	<14500	10500±500	<13000	11600±400	<11000
$n_e(\text{cm}^{-3})$	<10	1800±1000	<10	<10	<10	<30	<10	<10	<10	<10
410.1 H δ	25±2	-	20±3	-	17±2	19±2	27±2	29±2	24±1	21±3
434.0 H γ	44±2	-	44±4	-	37±	40±3	48±2	43±2	51±1	45±2
436.3 [O III]	<4	-	<3	-	<4	<2	1.3±0.3	<1.6	2.4±0.6	< 1.7
447.1 He I	-	-	-	-	-	-	-	-	5±1	-
486.1 H β	100±5	100±17	100±5	100±8	100±2	100±3	100±2	100±2	100±2	100±4
495.9 [O III]	38±2	84±19	22±4	181±11	71±2	19±2	59±1	38±1	90±2	71±3
500.7 [O III]	102±3	236±22	73±4	588±16	208±4	55±4	176±2	113±2	251±3	213±4
587.6 He I	11±2	-	8±2	-	17±2	11±2	15±1	13±1	16±1	13±2
631.2 [S III]	3.5±1.5	-	-	-	3±1.5	-	2 ± 1	3±2	3.6±0.4	3±2
654.8 [N II]	14±1	-	17±3	-	13±2	21±3	15±1	11±1	16.1±0.5	8±2
656.3 H α	296 ± 4	378±22	352±6	378±13	370±5	302±5	270±3	284±3	344 ± 2	293±5
658.4 [N II]	34±2	45±17	48±3	49±8	40±3	45±3	46±2	30±2	39±1	33±2
671.7 [S II]	33±2	26±14	77±4	71±7	45±2	55±2	31±1	21±2	29±1	33±3
673.1 [S II]	20±2	35±15	50±3	39±6	30±2	39±2	21±1	14±2	19.5±0.3	22±1
706.5 He I	-	-	-	-	-	-	6±1	3±2	4.5±0.8	-
713.5 [Ar III]	8.5±1.5	11±10	6±2	-	12±1	7±1	17±1	8±1	22.1±0.9	13 ± 2
732.0 [O II]	2.9±1	-	-	-	-	-	5.7±1	-	5.2±0.4	4.3±1
733.0 [O II]	1.0±1	-	-	-	-	-	3±1	-	6.4±0.4	4.2±1

	BCLMP289	BCLMP218	SNR15	BCLMP258b	BCLMP288a	CSPDP97	MCM00 E24	BCLMP220	CSPDP194	BCLMP256c
$c(\text{H}\beta)$	0.25±0.03	0.34±0.01	0.60±0.02	0.30±0.01	0.00±0.01	0.28±0.04	0.13±0.01	0.55±0.01	0.28±0.01	0.22±0.01
$T_e([\text{O III}])$ (K)	12500±1000	9800±200	-	-	-	-	10100±500	<14000	8900±500	-
$T_e([\text{N II}])$ (K)	-	-	-	-	-	-	-	-	8700±1000	-
$n_e(\text{cm}^{-3})$	<10	<30	<60	<10	<10	<10	<10	500±100	<20	<10
410.1 H δ	28±4	25.5±0.7	-	22±3	29±1	-	33±1	25±1	27.2±0.4	29±2
434.0 H γ	47±4	43.4±0.8	37±2	36±3	47±1	-	38±1	34±2	45.1±0.4	40±2
436.3 [O III]	4.5±1.5	1.3±0.2	-	-	-	-	1.1±0.3	<4	0.9±0.3	-
468.6 He II	-	-	-	4±3	-	-	-	2±1	-	-
486.1 H β	100±6	100±1	100±3	100±3	100±1	100±9	100±2	100±2	100±0.5	100±2
495.9 [O III]	122±6	86.1±0.8	41±2	131±3	64±1	211±10	56±1	102±1	78.2±0.4	51±1
500.7 [O III]	372±4	230±2	118±4	387±4	188±2	642±17	155±3	271±3	201.3±0.2	153±2
575.5 [N II]	-	-	-	-	-	-	-	-	0.35±0.1	-
587.6 He I	17±5	14.4±0.5	12±1	10±1	10±1	-	14±1	16±1	12.8±0.2	11±1
631.2 [S III]	9±4	2.3±0.4	-	-	-	-	1.4±1	-	1.3±0.1	-
654.8 [N II]	14±4	13.5±0.4	34±2	11±1	10±1	-	13±1	7±5	8.5±0.2	7±2
656.3 H α	340±7	361±2	435±5	353±3	270±2	347±11	314±3	420±3	340±1	327±4
658.4 [N II]	40±4	42.0±0.8	79±3	29±1	26 ± 1	43±7	38±1	26±1	25.1±0.3	27±2
671.7 [S II]	47±4	39±0.6	109±3	40±2	15±1	29±13	26±1	26±1	11.7±0.2	18±1
673.1 [S II]	33±4	28.0±0.6	80±3	26±2	10±1	20±13	17±1	25±1	8.3±0.2	12±1
706.5 He I	-	4.0±0.5	-	-	-	-	3±1	4±1	2.3±0.2	3±1
713.5 [Ar III]	9±5	14.6±0.5	12±1	11±2	8±1	22±4	12±1	16±1	13.3±0.2	11±2
732.0 [O II]	7 ± 4	2.4±0.3	-	-	-	-	1.8±2	-	1.9±0.2	-
733.0 [O II]	9±4	2.6±0.3	-	-	-	-	3.1±3	-	1.4±0.1	-

	VGHC2-22	BCLMP618b	CPSDP103	BCLMP638N	BCLMP626	CPSDP107	LGC HII 4	SNR25	BCLMP45	BCLMP207a
$c(\text{H}\beta)$	0.22±0.01	0.12±0.01	0.40±0.02	0.24±0.01	0.09±0.01	0.39±0.01	0.21±0.01	0.89±0.02	0.718±0.004	0.25±0.02
$T_e([\text{O III}])$ (K)	-	-	-	11000±500	11300±800	-	-	-	8600±200	-
$T_e([\text{N II}])$ (K)	-	-	-	-	-	-	-	-	8200±1000	-
$n_e(\text{cm}^{-3})$	<50	<10	<10	<20	<40	<10	<10	<30	<70	<100
410.1 H δ	21±1	31±1	21±4	28±1	37±1	-	-	-	19.7±0.4	-
434.0 H γ	39±1	50±1	46±2	43±1	44±1	40±2	33±3	30±5	39.1±0.5	-
436.3 [O III]	-	-	-	3.8±0.5	1.6±0.5	-	-	-	0.8±0.2	-
468.6 He II	-	-	-	-	-	-	-	-	1.4±0.2	-
486.1 H β	100±1	100±2	100±4	100±1	100±2	100±3	100±3	100±4	100±0.8	100±4
495.9 [O III]	54±1	30±1	21±3	162±2	61±2	89±3	85±3	29±5	94.0±0.8	90±6
500.7 [O III]	151±2	83±1	69±3	467±4	171±2	270±4	268±5	113±4	277±2	259±6
575.5 [N II]	-	-	-	-	-	-	-	-	0.4±0.1	-
587.6 He I	13±1	-	10±2	13.2±0.6	11±1	17±2	14±2	12±2	21.1±0.4	-
631.2 [S III]	-	-	-	2±0.5	3±1	-	3.8±3	-	2.5 ± 0.3	-
654.8 [N II]	10.3±0.6	10.6±0.5	20±3	6.4±0.6	10.2±0.5	13±1	15±2	49±4	13.7±0.2	33±4
656.3 H α	333±3	310±1	378±8	337±2	304±3	374±6	329±4	530±9	471±1	340±6
658.4 [N II]	31±1	39.8±0.7	49±3	14.7±0.7	29±1.5	23±2	49±2	163±6	36.4±0.6	103±4
671.7 [S II]	20.7±0.7	27.8±0.7	49±2	13.1±0.8	24±1	26±2	25±2	351±7	19.8±0.4	148±4
673.1 [S II]	15.1±0.7	18.6±0.8	34±2	9.3±0.6	17.4±0.7	17±2	17±2	252±6	14.7±0.4	112±5
706.5 He I	-	-	4±1	3.4±0.7	1.9±0.8	3±1	-	5±3	5.6±0.2	-
713.5 [Ar III]	9.8±0.6	-	9±1	13.1±0.7	9.0±0.7	15±1	8±1	13±3	27.8±0.4	-
732.0 [O II]	-	-	-	-	2.8±0.5	-	5±2	-	3.8±0.3	-
733.0 [O II]	-	-	-	-	3.7±0.5	-	4±2	-	3.2±0.2	-

Table 3. Total and ionic chemical abundances, and ionization correction factors of fourteen H II regions. The galactocentric distance in kpc is also reported.

radial distance (kpc)	LGC HII 2 6.5	LGC HII 3 5.8	BCLMP289 5.2	BCLMP218 4.2	MCM00Em24 5.7
He ⁺ /H ⁺	0.116±0.009	0.112±0.008	0.12±0.04	0.092±0.005	0.100±0.009
N ⁺ /H ⁺ ×10 ⁵	0.86±0.06	0.50±0.03	0.41±0.07	0.65±0.02	0.66±0.06
ICF(N)	1.73	1.76	1.82	2.39	1.9
28 N/H×10 ⁵	1.5±0.9	0.88±0.34	0.8±0.9	1.5±0.5	1.3±0.5
12 + log N/H	7.17±0.25	6.94±0.17	6.90±0.50	7.19±0.14	7.10±0.30
O ⁺ /H ⁺ ×10 ⁵	12±5	12±3	11.8±10	8.9±2.9	9.5±10
O ⁺⁺ /H ⁺ ×10 ⁵	5.5±0.9	5.6±0.7	6.1±2.	8.9±0.6	5.4±1.5
O/H×10 ⁵	17.5±6.0	17.6±4.	18.±12	17.8±3.5	15.0±11.
12 + log O/H	8.25 ±0.06	8.24±0.05	8.25±0.13	8.25±0.05	8.18±0.25
S ⁺ /H ⁺ ×10 ⁶	1.2±0.1	0.62±0.05	0.8±0.1	1.2±0.4	0.9±0.1
S ⁺⁺ /H ⁺ ×10 ⁶	4.7±2.0	3.7±0.9	6.3±4.3	4.7±1.6	2.9±1.5
ICF(S)	1.0	1.0	1.0	1.01	1.0
S/H×10 ⁶	5.9±3.9	4.3±1	7.1±4.4	5.9±2.0	3.8±1.6
12 + log S/H	6.75±0.18	6.62±0.11	6.85±0.3	6.77±0.15	6.55±0.3
Ar ⁺⁺ /H ⁺ ×10 ⁶	1.5±0.2	1.3±0.5	0.4±0.3	1.0±0.2	0.9±1.7
ICF(Ar)	1.20	1.18	1.16	1.10	1.20
Ar/H×10 ⁶	1.8±0.6	1.5±1.4	0.3±0.6	1.1±0.2	1.1±1.3
12 + log Ar/H	6.26 ±0.14	6.18±0.40	5.70±0.60	6.10±0.10	6.04±0.50
radial distance (kpc)	CPSDP194 4.2	BCLMP626 5.8	BCLMP45 2	BCLMP637 4.7	GDK99 128 2.2
He ⁺ /H	0.083±0.003	0.085±0.01	0.108±0.005	0.087±0.017	0.0980±0.004
He ⁺⁺ /H ⁺ ×10 ²			0.13±0.02		
N ⁺ /H ⁺ ×10 ⁵	0.48±0.05	0.42±0.05	0.58±0.03	0.34±0.03	1.1±0.1
ICF(N)	2.70	1.74	2.49	5.80	1.92
N/H×10 ⁵	1.33±0.60	0.73±0.50	14.7±5	19.7±10	2.0±1.0
12 + log N/H	7.12±0.20	6.86±0.30	7.17±0.15	7.30±0.40	7.31±0.21
O ⁺ /H ⁺ ×10 ⁵	8.0±3.0	9.3±4.3	14.3±5.0	3.5±3.0	18.4±6.0
O ⁺⁺ /H ⁺ ×10 ⁵	10.6±2.2	4.2±0.9	16.2±2.0	18.5±2.0	11.0±2.0
O/H×10 ⁵	18.6±5.2	13.5±5.2	30.5±7.0	22.0±5.	29.4±8.0
12 + log O/H	8.27±0.06	8.13±0.07	8.49±0.04	8.34±0.05	8.47±0.06
S ⁺ /H ⁺ ×10 ⁶	0.5±0.1	0.65±0.08	0.67±0.05	0.61±0.05	1.3±0.3
S ⁺⁺ /H ⁺ ×10 ⁶	4.0±1.3	3.7±2.5	7.5±2.7	4.3±3.	8.3±3.7
ICF(S)	1.05	1.00	1.01	1.60	1.00
S/H×10 ⁶	4.6±1.8	4.3±2.6	8.3±3.2	7.7±7	9.6±4.0
12 + log S/H	6.67±0.17	6.61±0.28	6.92±0.17	6.90±0.40	6.98±0.21
Ar ⁺⁺ /H ⁺ ×10 ⁶	1.3±0.2	0.57±0.08	1.9±0.1	1.1±0.1	1.6±0.2
ICF(Ar)	1.08	1.20	1.10	1.10	1.15
Ar/H×10 ⁶	1.4±0.4	0.68±0.28	2.1±0.4	1.7±0.5	1.8±0.5
12 + log Ar/H	6.13±0.12	5.83±0.18	6.32±0.10	6.09±0.17	6.25±0.13
radial distance (kpc)	BCLMP670 3.5	VGHC 2-84 2.4	BCLMP717b 4.6	LGC HII 11 7.2	BCLMP638N 6.5
He ⁺ /H	0.133±0.014	0.109±0.005	0.0851±0.006	0.093±0.01	0.091±0.06
N ⁺ /H ⁺ ×10 ⁵	0.92±0.09	0.58±0.03	0.56±0.04	0.26±0.03	0.21±0.02
ICF(N)	1.50	1.50	1.95	1.90	-
N/H×10 ⁵	1.4±1	0.9±0.4	1.1±0.7	0.48±0.28	-
12 + log N/H	7.14±0.30	6.95±0.18	7.04±0.28	6.68±0.26	-
O ⁺ /H ⁺ ×10 ⁵	14.6±6	17.±4	9.3±4.7	9.6±4.0	-
O ⁺⁺ /H ⁺ ×10 ⁵	4.4±1	5.3±0.7	5.7±1.1	5.2±1.0	12.0±0.6
O/H×10 ⁵	19.0±7	22.3±4.7	15.0±5.8	14.8±5.0	-
12 + log O/H	8.28±0.07	8.35±0.04	8.18±0.07	8.17±0.06	-
S ⁺ /H ⁺ ×10 ⁶	0.70±0.13	0.72±0.04	0.76±0.08	0.37±0.05	0.33±0.08
S ⁺⁺ /H ⁺ ×10 ⁶	5.0±2.0	3.3±1.0	3.1±1.8	2.3±2.1	1.9±2.
ICF(S)	1.0	1.0	1.0	1.0	-
S/H×10 ⁶	5.7±2.1	3.7±1.0	3.8±2.2	2.7.±2.2	-
12 + log S/H	6.75±0.18	6.56±0.12	6.57±0.24	6.42±0.40	-
Ar ⁺⁺ /H ⁺ ×10 ⁶	1.4±0.2	0.97±0.1	0.95±0.1	0.54±0.10	-
ICF(Ar)	1.20	1.20	1.10	1.10	-
Ar/H×10 ⁶	1.7±0.7	1.2±0.3	1.1.±4.	6.3±2.6	-
12 + log Ar/H	6.24 ±0.17	6.07±0.10	6.04±0.16	5.97±0.18	-

Table 4. Total and ionic chemical abundances, and ionization correction factors of H II regions with line fluxes from previous observations and with electron temperature diagnostic lines detected: KW81 (Kwitter & Aller 1981), V88 (Vilchez et al. 1988), C06 (Crockett et al. 2006). In case of multiple observations by different authors we used the most recent ones. The galactocentric distance in kpc is also reported.

	NGC595 (V88)	MA2 (V88)	NGC604 (V88)	IC131 (V88)	NGC588 (V88)
radial distance (kpc)	1.7	2.4	3.5	3.9	5.6
He ⁺ /H ⁺	0.07±0.05	0.075±0.003	0.082±0.002	0.080±0.009	0.09±0.01
N ⁺ /H ⁺ ×10 ⁵	1.43±0.08	0.70±0.05	0.93±0.02	0.64±0.07	0.18±0.02
ICF(N)	2.0	2.3	2.4	3.1	4.0
N/H×10 ⁵	2.9±0.6	1.6±0.4	2.2±0.1	2.0±0.4	0.74±0.65
12 + log N/H	7.4±0.1	7.21±0.10	7.35±0.02	7.30±0.09	6.87±0.04
O ⁺ /H ⁺ ×10 ⁵ (372.7)	17±2.5	12.5±2	15.4±0.5	9.9±1.2	5.8±0.3
O ⁺ /H ⁺ ×10 ⁵ (732.5)	16.5±3	-	17.5±2.4	-	-
O ⁺⁺ /H ⁺ ×10 ⁵	11.9±2.	11.6±2.	15.3±0.7	17.0±0.3	16.7±1.1
O/H×10 ⁵ (372.7)	28.9±4.	24.±5	30.7±1.3	26.8±4.7	22.5±1.4
O/H×10 ⁵ (732.5)	28.4±5.	-	32.8±3.0	-	-
12 + log O/H (372.7)	8.46±0.08	8.38±0.04	8.49±0.02	8.43±0.03	8.35±0.02
12 + log O/H (732.5)	8.45±0.09	-	8.52±0.04	-	-
S ⁺ /H ⁺ ×10 ⁶	1.0±0.1	0.9±0.1	1.3±0.1	1.1±0.1	0.41±0.04
S ⁺⁺ /H ⁺ ×10 ⁶	5.2±2	4.9±2	8.1±0.5	-	6.8±1.3
ICF(S)	1.0	1.0	1.01	-	1.2
S/H×10 ⁶	6.0±2.	5.8±2.0	9.4±0.6	-	8.64±1.8
12 + log S/H	6.9±0.2	6.8±0.1	6.97±0.05	-	6.94±0.17
Ar ⁺⁺ /H ⁺ ×10 ⁶	1.3±0.1	1.1±0.1	1.3±0.07	-	0.9±0.1
ICF(Ar)	1.14	1.11	1.11	-	1.06
Ar/H×10 ⁶	1.5±0.3	1.2±0.3	1.5±0.1	-	0.9±0.1
12 + log Ar/H	6.2±0.1	6.1±0.1	6.8±0.7	-	6.0±0.1
radial distance (kpc)	MA 3 (KW81)	IC 133 (KW81)	IC 132 (KW81)	BCLMP90 (C06)	BCLMP691 (C06)
	3.2	5.5	6.4	1.3	3.3
He ⁺ /H	0.083±0.02	0.078±0.02	0.11±0.02	-	-
N ⁺ /H ⁺ ×10 ⁵	0.37±0.08	0.18±0.04	0.89±0.32	-	-
ICF(N)	3.6	4.3	5.3	-	-
N/H×10 ⁵	1.3±0.8	7.7±2.6	4.7±1.8	-	-
12 + log N/H	7.11±0.28	6.89±0.14	6.7±0.2	-	-
O ⁺ /H ⁺ ×10 ⁵ (372.7)	8.5±3.6	4.1±0.7	2.2±0.3	8.2±1.2	6.7±0.5
O ⁺ /H ⁺ ×10 ⁵ (732.5)	8.1±8.0	5.6±3.6	-	-	-
O ⁺⁺ /H ⁺ ×10 ⁵	19±10	12.8±3.0	9.9±2.0	24.4±4.7	12.3±1.5
O/H×10 ⁵ (372.7)	28±14	16.9±4.3	12.1±2.6	32.5±6.0	19.0±2
O/H×10 ⁵ (732.5)	27±18	18.4±7.2	-	-	-
12 + log O/H (372.7)	8.45±0.10	8.23±0.05	8.08±0.04	8.51±0.04	8.28±0.03
12 + log O/H (732.5)	8.44±0.12	8.26±0.08	-	-	-
S ⁺ /H ⁺ ×10 ⁶	0.34±0.12	0.18±0.05	0.15±0.04	-	-
S ⁺⁺ /H ⁺ ×10 ⁶	-	1.8±1.5	-	-	-
ICF(S)	-	1.3	-	-	-
S/H×10 ⁶	-	2.5±2.1	-	-	-
12 + log S/H	-	6.4±0.4	-	-	-
Ar ⁺⁺ /H ⁺ ×10 ⁶	0.9±0.3	0.7±0.1	0.4±0.1	-	-
ICF(Ar)	1.06	1.1	1.10	-	-
Ar/H×10 ⁶	0.9±0.5	0.7±0.2	0.4±0.1	-	-
12 + log Ar/H	6.0±0.2	5.9±0.1	5.6±0.2	-	-
radial distance (kpc)	BCLMP745 (C06)	BCLMP706 (C06)	BCLMP290 (C06)	MA1 (C06)	-
	4.6	5.6	4.2	7.4	-
O ⁺ /H ⁺ ×10 ⁵	7.3±2	12.9±5.4	9.7±1.2	3.6±0.3	-
O ⁺⁺ /H ⁺ ×10 ⁵	5.1±1.6	9.2±4.4	7.4±1.2	14.6±2.2	-
O/H×10 ⁵	12.5±3.5	22.2±9.8	17.1±2.5	18.2±2.6	-
12 + log O/H	8.09±0.05	8.34±0.08	8.23±0.05	8.26±0.05	-